Enhanced Compensation Filter to Mitigate Subsynchronous Oscillations in Series-Compensated DFIG-Based Wind Farms

Andres E. Leon, *Senior Member, IEEE*, Santiago J. Amodeo, and Juan Manuel Mauricio, *Senior Member, IEEE*

***Abstract*—This paper presents a control strategy to mitigate subsynchronous oscillations (SSOs) in doubly-fed induction generator (DFIG)-based wind farms integrated into series-compensated transmission systems. The strategy has two parts: in the first one, a compensation filter based on the motion-induction amplification concept is proposed to increase the damping of the DFIG machine in the subsynchronous frequency range; in the second one, a proportional-integral (PI)-like controller is designed using an optimal quadratic technique to minimize the control effort and the additional rotor voltage required by the SSO damping action. The SSO mitigation strategy acts locally on the DFIG control system reducing the negative resistance the rotating machine presents to the grid at subsynchronous frequencies; this approach reduces the control dependence on the topology and resonance frequencies of the network. The control strategy is validated with a case study based on the Argentinian power system and evaluated in a wide range of operating conditions, showing that the DFIG control system can be enhanced to mitigate poorly damped SSOs and increase the penetration level of wind power in the system.**

***Index Terms*—Resonance mitigation, series capacitor, series compensation, subsynchronous resonance (SSR), wind energy conversion systems (WECS), wind power integration.**

I. Introduction

THE development of large-scale wind and solar projects and the growing energy demand require that the power transmission capacity of the system be correspondingly increased. The transmission infrastructure also needs to be updated to cope with renewable energy sources located far from the main load centers [1]. Series compensation of existing lines using fixed capacitors is one of the most cost-effective solutions to increase transmission capacity. In this context, the construction of wind farms near series-compensated transmission lines is more and more frequent [2].

A series-compensated transmission line has a resonance frequency for both positive and negative sequence components. In a synchronous reference frame, these resonances are seen as subsynchronous and supersynchronous modes. Because the doubly-fed induction generator (DFIG) and its controller exhibit a negative resistance at subsynchronous frequencies, the damping of the subsynchronous mode is reduced by the presence of a nearby DFIG-based wind farm [3]. In the literature, the interaction between the wind turbine control system and a series-compensated transmission system has been called subsynchronous control interaction (SSCI) [4]–[6], and it has received considerable attention in the last years since subsynchronous oscillations (SSOs) were observed in series-compensated DFIG-based wind farms (see a review of the SSCI events occurred in real systems in [7]–[9]).

Different approaches have been proposed to mitigate SSCI. The use of bypass filters and flexible ac transmission systems is examined in [10]. The main drawback of implementing these approaches is the high cost of the required equipment. To reduce costs, a shunt converter with reduced rating operating only at the subsynchronous frequency is presented in [11]. Modifications in the DFIG control system have also been considered; for example, the reduction of the current control bandwidth and the inclusion of notch filters are analyzed in [1] and [12], respectively. In the first case, attention has to be paid not to excessively reduce the dynamic response of the DFIG under disturbances, deteriorating the fault ride-through capability; in the second case, the notch filter needs to accurately extract the subsynchronous frequency to operate properly.

Another approach consists of including a supplementary damping control (SDC) in the DFIG control system. SDCs can use local or remote measurements [13]; they act on the grid-side converter (GSC) [13]–[16], rotor-side converter (RSC) [17]–[21], or both converters [22]–[24]; and they are implemented in a centralized manner (park level) or decentralized manner (distributed in each wind turbine) [23]. All of them have advantages and disadvantages in terms of complexity, tuning procedure, and damping capacity; for example, controls based on remote measurements must deal with communication delays, whereas centralized schemes must coordinate the individual

Manuscript received August 25, 2020; revised December 7, 2020; accepted
Q1 January 2, 2021. This work was supported in part by the Consejo Nacional de Investigaciones Científicas y Técnicas (CONICET), in part by the Spanish Ministry of Economy, and Competitiveness under Grant ENE2017-84813-R, and in part by the European Union Horizon 2020 Program under Grant 764090. Paper no. TPWRD-01309-2020. *(Corresponding author: Andres E. Leon.)*

Q2 Andres E. Leon is with the Instituto de Investigaciones en Ingeniería Eléctrica (IIIE) "Alfredo Desages," Universidad Nacional del Sur (UNS)-CONICET, Bahía Blanca 8000, Argentina (e-mail: andreseleon@gmail.com).

Santiago J. Amodeo is with the ElectroAMSA Company and Universidad Nacional del Sur (DIEC-UNS), Bahía Blanca 8000, Argentina (e-mail: samodeo@uns.edu.ar).

Juan Manuel Mauricio is with the Department of Electrical Engineering, Universidad de Sevilla, 41092 Sevilla, Spain (e-mail: j.m.mauricio@ieee.org).

Color versions of one or more figures in this article are available at https://doi.org/10.1109/TPWRD.2021.3049318.

Digital Object Identifier 10.1109/TPWRD.2021.3049318

wind turbines. SDC designs are mainly based on lead-lag compensators (see [10] and [15]–[18]), but other approaches using a high-pass filter with proportional control [13], linear quadratic regulator (LQR) [21]–[23], and nonlinear control [19] can also be found in the literature. To reduce the dependence of the controller parameters on the network model and the system operating point, the SDC is usually designed for the worst-case scenario [22]–[24] (i.e., the operating point with lower SSO damping). SDCs designed using optimization algorithms and based on gain scheduling techniques are also implemented to improve the control performance for different operating points (see [11], [17] and [25]). A detailed comparison of different SSCI mitigation techniques can be found in [10]. On the other hand, the motion-induction amplification (MIA) concept is considered in [26] to compensate SSCI. This concept can be interpreted as the representation of the machine slip in the Laplace domain (see [27] and [28]). It allows understanding the root of the SSCI problem by studying how elements of the rotor are seen from the stator terminals and enables an SSCI countermeasure with a lower dependence on the network parameters and the system operating point.

In [26], a compensation filter with a damping term is added to the rotor current controller to mitigate SSCI. This filter impacts on the rotor voltage dynamics, and the damping ratio of the introduced eigenvalues needs to be chosen to avoid excessive oscillations and overshoots in the rotor voltage. In our work, it is shown that one of the closed-loop filter eigenvalues cannot be properly damped by a compensation filter with a single damping term; therefore, we enhanced the filter by introducing a second damping parameter that directly damps this critical eigenvalue, improving the system response during the SSCI mitigation. A proportional-integral (PI)-like controller with cross-decoupling terms obtained with the LQR method is also designed to optimize the use of the control signal (i.e., the rotor voltage).

The contribution of this paper is an enhancement of the control strategy recently proposed in [26] to mitigate SSOs in series-compensated DFIG-based wind farms. Unlike the previous work, we propose a compensation filter with double damping terms to improve the damping and increase the flexibility to adjust the required control action. This additional degree of freedom allows reducing oscillations and overshoots in the rotor voltage when using the compensation filter, improving its practical implementation. Eigenvalue (modal) analysis is used to assess the impact of the filter parameters on the system dynamics and provide guidelines to select their values. The strategy uses local measurements to reduce communication delays, and it is added to the DFIG control system (i.e., a software modification) to avoid the costs of additional hardware and equipment. The effectiveness of the proposed approach is validated with a practical multi-machine power system with several wind farms and multiple series-compensated lines.

II. Motion-Induction Amplification Concept

In this section, the MIA concept is briefly described for the sake of completeness (see [26] for further details). The DFIG model in complex notation and in the $\alpha\beta$ stationary reference frame is first considered

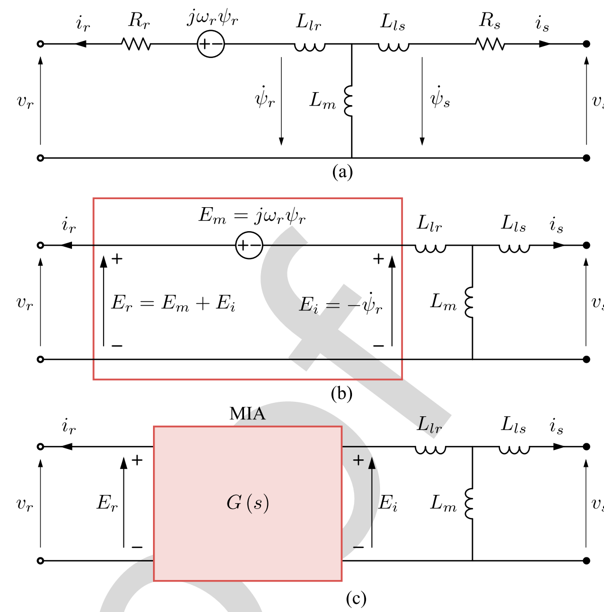

Fig. 1. Equivalent electric circuit of the DFIG and the MIA concept.

$$v_s = -R_s i_s - \dot{\psi}_s \tag{1}$$

$$v_r = -R_r i_r + j\omega_r \psi_r - \dot{\psi}_r \tag{2}$$

$$\psi_s = L_m (i_s + i_r) + L_{ls} i_s \tag{3}$$

$$\psi_r = L_m (i_s + i_r) + L_{lr} i_r \tag{4}$$

where voltage, current, and flux signals are denoted by $v = v_\beta + jv_\alpha$, $i = i_\beta + ji_\alpha$, and $\psi = \psi_\beta + j\psi_\alpha$, respectively, and the subscripts s and r stand for stator and rotor quantities [the rest of the parameters are shown in Fig. 1(a)].

The motional EMF generated by the rotation of the rotor $E_m = j\omega_r\psi_r$ and the induced EMF generated by the variation of the flux $E_i = -\dot{\psi}_r$ are identified in Fig. 1(b); resistances are not shown for simplicity. A two-port network with input voltage $E_r = E_m + E_i$ and output voltage E_i can be defined as shown in Fig. 1(c). The gain (or amplification) from the input E_r to the output E_i is given by

$$G = \frac{E_i}{E_r} = \frac{E_i}{E_m + E_i} = \frac{-\dot{\psi}_r}{j\omega_r\psi_r - \dot{\psi}_r} \tag{5}$$

and applying the Laplace transform yields

$$G(s) = \frac{-s\psi_r}{j\omega_r\psi_r - s\psi_r} = \frac{s}{s - j\omega_r}. \tag{6}$$

The transfer function $G(s)$ is key to understand and compensate the poorly damped SSOs observed in series-compensated DFIG-based wind farms.

Bode plots of $G(s)$ for two values of rotor speed are shown in Fig. 2. In both cases, a negative gain (i.e., a 180° phase shift) is observed in the frequency range from 0 to ω_r, and hence in the typical frequency range of network subsynchronous resonances. This result can also be verified by replacing the operator s by $j\omega$ in (6) obtaining $G(j\omega) = \frac{\omega}{\omega - \omega_r}$, which takes negative values

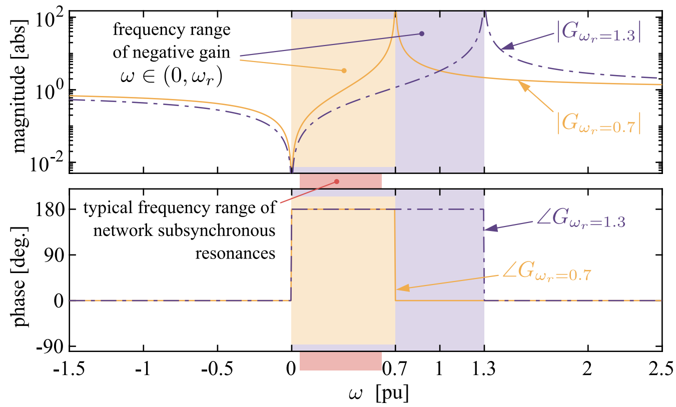

Fig. 2. Bode plots of $G(s)$ for $\omega_r = 0.7$ pu and $\omega_r = 1.3$ pu (solid yellow line and dot-dashed purple line, respectively).

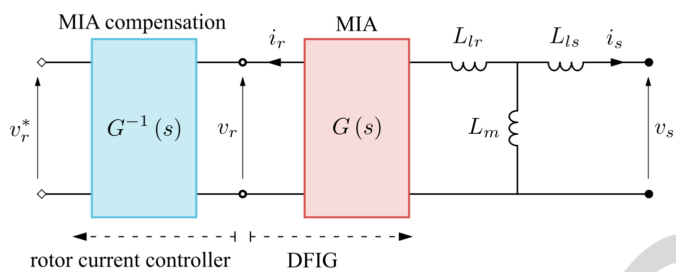

Fig. 3. Ideal compensation of the MIA effect.

in the frequency range $\omega \in (0, \omega_r)$. Therefore, elements on the rotor side such as the rotor resistance and the proportional gain of the rotor current controller are seen as negative from the stator terminals [3], consequently reducing the SSO damping of the system. Fig. 2 also shows that the gain of $G(s)$ is higher in the subsynchronous frequency range for the case with a lower rotor speed, which agrees with previous studies indicating that the SSO damping is further reduced at low rotor speeds [27].

To compensate the MIA effect, the inverse of the transfer function (6) can be multiplied at the output of the rotor current controller as shown in Fig. 3. This ideal compensation is given by

$$\frac{v_r(s)}{v_r^*(s)} = G^{-1}(s) = \frac{s - j\omega_r}{s} \tag{7}$$

where an auxiliary rotor voltage v_r^* is defined. Because the transfer function (7) affects the dynamics of the DFIG control system, a damping term must be added to reduce any adverse interaction. In [26], this damping term is included only in the numerator (the zero) of the transfer function (7). In our work, we show that by including damping terms in both the numerator and the denominator, a higher flexibility to mitigate SSOs and control the rotor voltage response is achieved.

III. Control Strategy to Mitigate SSOs

A. *Compensation Filter*

The following transfer function based on (7) with double damping terms σ_z and σ_p is proposed to compensate the MIA

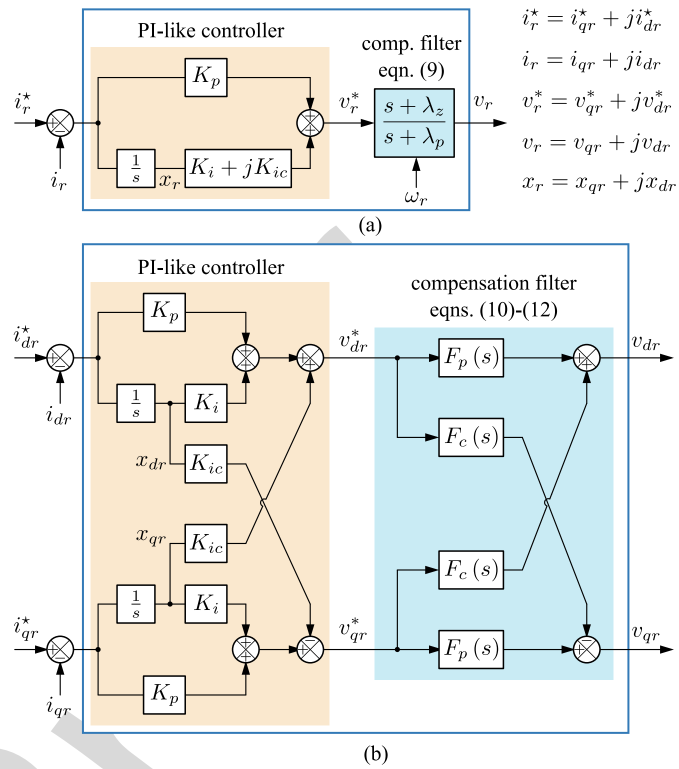

Fig. 4. Block diagram of the proposed SSO mitigation strategy. (a) Complex notation and (b) scalar notation.

effect

$$\frac{v_r(s)}{v_r^*(s)} = H_{\alpha\beta}(s) = \frac{s - j\omega_r + \sigma_z}{s + \sigma_p}. \tag{8}$$

The transfer function (8) works as a filter at the output of the rotor current controller, hereinafter called compensation filter. This filter in the $\alpha\beta$ stationary reference frame is converted to the dq synchronous reference frame to be compatible with the rotor current controller also designed in dq coordinates. This can be done using the transformation $v_{\alpha\beta} = e^{j\theta_s} v_{dq}$ or simply replacing the operator s by $s + j\omega_s$ in (8), yielding

$$\frac{v_r(s)}{v_r^*(s)} = H_{dq}(s) = \frac{s + \sigma_z + j(\omega_s - \omega_r)}{s + \sigma_p + j\omega_s} = \frac{s + \lambda_z}{s + \lambda_p} \tag{9}$$

where $\lambda_z = \sigma_z + j(\omega_s - \omega_r)$ and $\lambda_p = \sigma_p + j\omega_s$. Note that the compensation filter uses the measurement of the rotor speed ω_r to adapt its behavior to different operating conditions of the DFIG, and it does not depend on the network and machine parameters. The transfer function (9) in complex notation can be written in scalar notation as follows

$$\begin{bmatrix} v_{dr}(s) \\ v_{qr}(s) \end{bmatrix} = \begin{bmatrix} F_p(s) & F_c(s) \\ -F_c(s) & F_p(s) \end{bmatrix} \begin{bmatrix} v_{dr}^*(s) \\ v_{qr}^*(s) \end{bmatrix} \tag{10}$$

where

$$F_p(s) = \frac{(s + \sigma_z)(s + \sigma_p) + \omega_s(\omega_s - \omega_r)}{(s + \sigma_p)^2 + \omega_s^2} \tag{11}$$

$$F_c(s) = \frac{(s + \sigma_p)(\omega_s - \omega_r) - (s + \sigma_z)\omega_s}{(s + \sigma_p)^2 + \omega_s^2}. \tag{12}$$

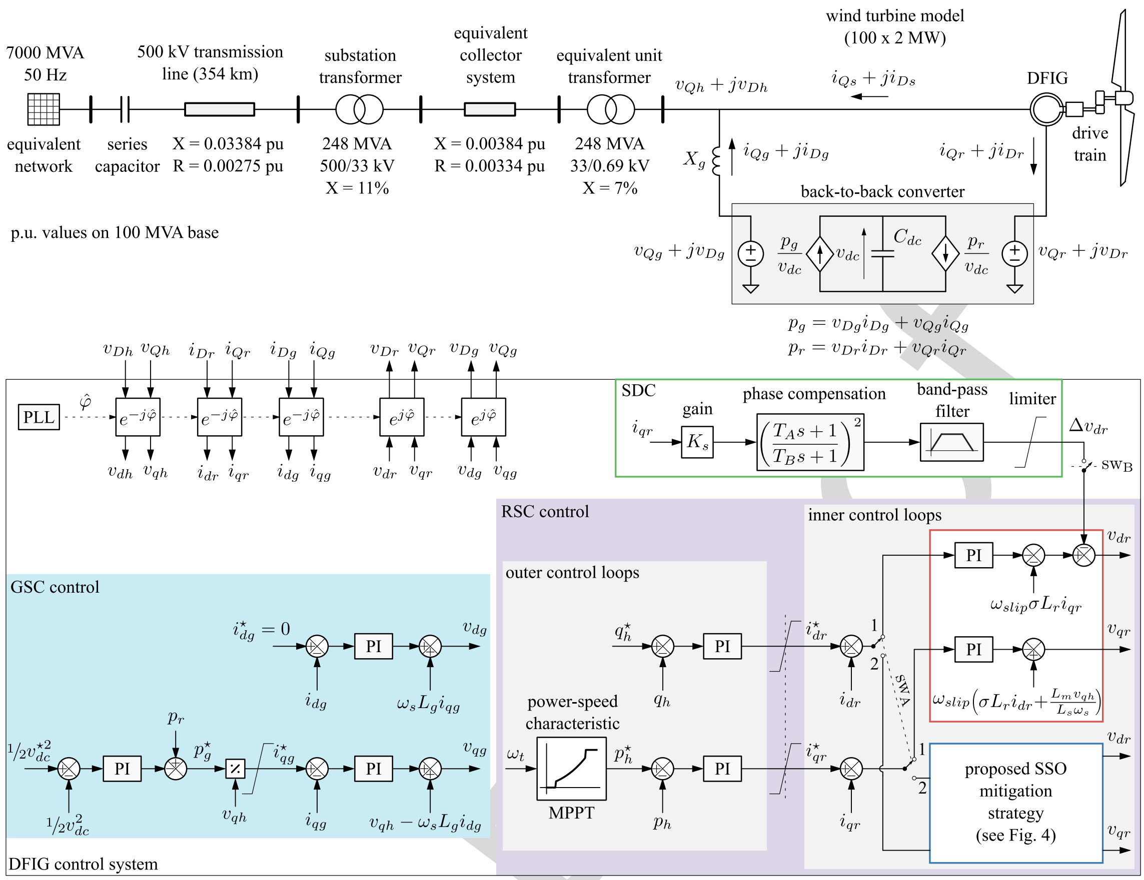

Fig. 5. Introductory case study based on a DFIG-based wind farm connected to the grid through a series-compensated transmission line (at the top) and block diagram of the DFIG control system with the considered control modification (at the bottom).

The selection of parameters σ_z and σ_p will be discussed in Section IV-B.

B. Rotor Current Controller

The DFIG model in the dq synchronous reference frame is given by

$$v_s = -R_s i_s - j\omega_s\psi_s - \dot{\psi}_s \tag{13}$$

$$v_r = -R_r i_r - j\left(\omega_s-\omega_r\right)\psi_r - \dot{\psi}_r \tag{14}$$

$$\psi_s = L_m\left(i_s+i_r\right)+L_{ls}i_s \tag{15}$$

$$\psi_r = L_m\left(i_s+i_r\right)+L_{lr}i_r \tag{16}$$

where voltage, current, and flux signals are denoted by $v = v_q + jv_d$, $i = i_q + ji_d$, and $\psi = \psi_q + j\psi_d$, respectively. Using (13)–(16), the rotor current dynamics can be expressed as follows

$$L_\sigma\dot{i}_r = -R_r i_r - j\omega_s L_\sigma i_r + \underbrace{j\omega_r\psi_r}_{\text{MIA}} + \frac{L_m}{L_s}\left(v_s+R_s i_s\right) - v_r \tag{17}$$

where the MIA term appears explicitly, and the total leakage factor $\sigma = 1 - L_m^2/[(L_m+L_{ls})(L_m+L_{lr})]$ and the parameter $L_\sigma = (L_m+L_{lr})\sigma$ are used. Because the MIA term is compensated by the compensation filter, the rotor current dynamics (17) can be rewritten as follows

$$\dot{i}_r = a i_r + b v_r^* + d \tag{18}$$

where the auxiliary voltage v_r^* is now the control input, $d = \frac{L_m}{L_\sigma L_s}(v_s+R_s i_s)$ is a disturbance, and $a = -\frac{R_r}{L_\sigma} - j\omega_s$ and $b = -\frac{1}{L_\sigma}$. The system (18) is extended with the integral of the current error to guarantee a zero steady-state error. The integrator dynamics is given by $\dot{x}_r = i_r - i_r^\star$; when combining it with (18), it results

$$\dot{\mathbf{x}}_e = \mathbf{A}_e\mathbf{x}_e + \mathbf{B}_e v_r^* - \begin{bmatrix}0\\1\end{bmatrix} i_r^\star \tag{19}$$

with extended state vector $\mathbf{x}_e = [\,i_r \;\; x_r\,]^T$ and matrices

$$\mathbf{A}_e = \begin{bmatrix}a & 0\\ 1 & 0\end{bmatrix}, \qquad \mathbf{B}_e = \begin{bmatrix}b\\0\end{bmatrix}. \tag{20}$$

Then, the following state-feedback controller is implemented

$$v_r^* = -\mathbf{K}\mathbf{x}_e. \tag{21}$$

An optimal quadratic technique (LQR) is chosen to design the control gain matrix $\mathbf{K}$. This technique minimizes the control efforts and allows a systematic design (see [29] for details of this technique). For the particular case of the matrices (20), the

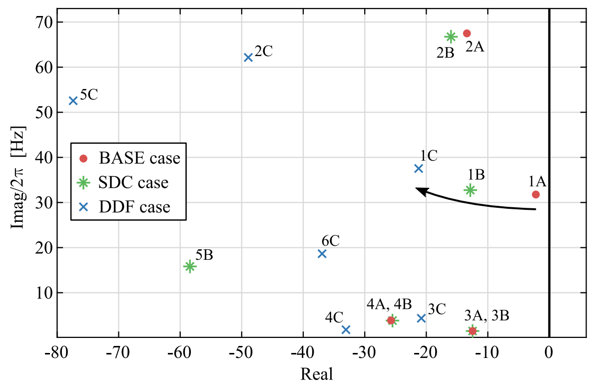

Fig. 6. System eigenvalues and location of the critical subsynchronous mode for different control approaches. Eigenvalue classification: {1A, 1B, 1C}: subsynchronous mode; {2A, 2B, 2C}: supersynchronous mode; {3A, 3B, 3C}: mode of the rotor current control loop; {4A, 4B, 4C}: phase-locked loop (PLL) mode; 5B: mode of the SDC filter; 5C and 6C: first and second modes of the compensation filter.

solution of the LQR problem gives the gain matrix

$$\mathbf{K} = \left[K_p \; K_i + jK_{ic} \right] \tag{22}$$

resulting in the control law

$$v_r^* = -K_p \left(i_r - i_r^{\star} \right) - \left(K_i + jK_{ic} \right) x_r \tag{23}$$

where $x_r = x_{qr} + jx_{dr}$ is the previously defined integrator state. The controller (23) has a structure similar to the one of a PI controller, but it uses a complex integral gain. PI structures are simple to implement and robust to parametric variations. Block diagrams of the proposed control strategy to mitigate SSOs considering both complex and scalar notations are shown in Fig. 4.

IV. Introductory Case Study

First, a DFIG-based wind farm connected to the grid through a series-compensated transmission line is analyzed to introduce the main concepts. Different control approaches are considered (see Fig. 5): a conventional vector control [30] (BASE case; switch $\mathrm{sw_A}$ in position 1 and switch $\mathrm{sw_B}$ disconnected), a vector control with an SDC based on lead-lag compensators [18] (SDC case; switch $\mathrm{sw_A}$ in position 1 and switch $\mathrm{sw_B}$ connected), and the proposed compensation filter with double damping terms (DDF case; switch $\mathrm{sw_A}$ in position 2 and switch $\mathrm{sw_B}$ disconnected). For comparison purposes, the approach introduced in [26] using a compensation filter with a single damping term (SDF case) is implemented by setting the parameter σ_p to zero.

Nonlinear time-domain simulations and eigenvalue analysis are performed in MATLAB using the approach described in [31].

A. Small-Signal (Modal) Analysis

Fig. 6 shows the system eigenvalues for the BASE, SDC, and DDF cases; the main eigenvalues (modes) are labeled using the participation factors. In this test, the DFIG is operating at the maximum power, and the transmission line has a compensation level of 70%. The parameters of the DDF case are selected as described in Section IV-B. In the BASE case, a poorly damped subsynchronous mode is observed (eigenvalue indicated with a red dot and labeled as 1A in Fig. 6). In the SDC and DDF cases, this critical mode is moved toward the left, increasing its damping ratio. A higher negative real part (i.e., higher damping ratio) is achieved in the DDF case for this subsynchronous mode (eigenvalue 1C).

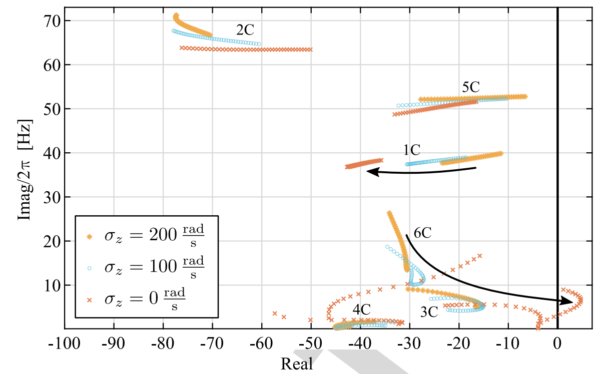

Fig. 7. Eigenvalues of the introductory case study for three values of σ_z, with $\sigma_p = 0$. Effect of the parameter σ_z on the modes 1C and 6C.

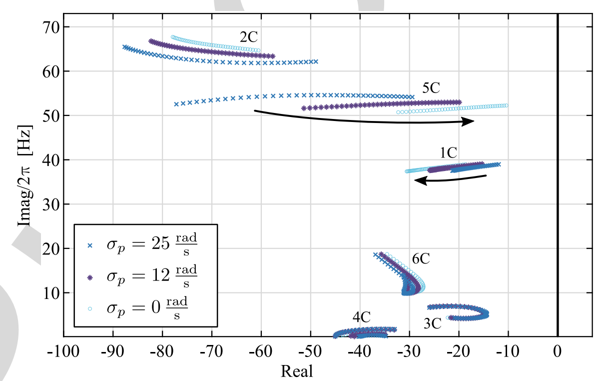

Fig. 8. Eigenvalues of the introductory case study for three values of σ_p, with $\sigma_z = 100$. Effect of the parameter σ_p on the modes 1C and 5C.

B. Selection of Compensation Filter Parameters

Fig. 7 shows the eigenvalues of the introductory case study covering operating points from low to high wind speeds with the transmission line compensated at 70%; three cases of the parameter σ_z are shown, considering $\sigma_p = 0$. A low value of parameter σ_z is desired so that the transfer function (8) is close to the transfer function (7), which allows a better MIA compensation and increases the DFIG damping in the subsynchronous frequency range (i.e., higher damping of the mode 1C). On the other hand, as the parameter σ_z is lowered, the compensation filter interacts with the DFIG control system degrading the stability of the mode 6C (see the arrow on the mode 6C in Fig. 7). Therefore, the selection of the parameter σ_z is a trade-off between avoiding the interaction of the compensation filter with the DFIG control system and reducing the SSOs (i.e., between having a stable mode 6C and increasing the damping of the mode 1C). In Fig. 7, this trade-off is seen in the movement in opposite directions of the modes 1C and 6C.

Fig. 8 shows the eigenvalues of the introductory case study for the same operating conditions of Fig. 7, but now three cases of the

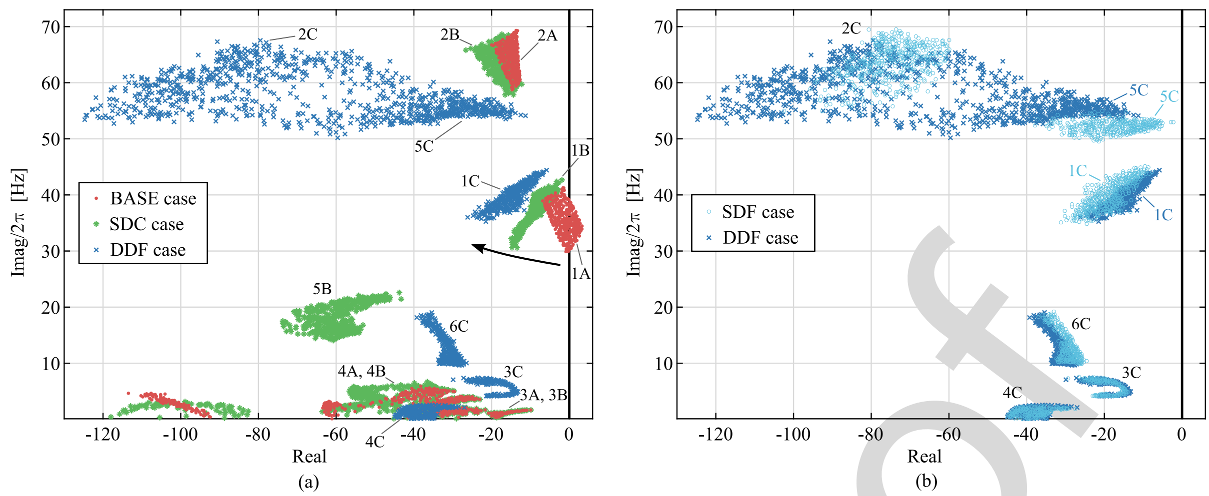

Fig. 9. System eigenvalues calculated for 1000 operating points corresponding to different wind powers, series compensation levels, and voltages of the network bus. (a) BASE, SDC, and DDF cases are shown with red dots, green asterisks, and blue crosses, respectively. (b) SDF and DDF cases are shown with light-blue circles and blue crosses, respectively.

parameter σ_p are shown, considering $\sigma_z = 100$. Similarly to the previous analysis, the parameter σ_p has to be as low as possible to obtain a close match between the transfer functions (7) and (8). However, as the parameter σ_p is lowered, the compensation filter interacts with the electrical network decreasing the damping of the mode 5C (see the arrow on the mode 5C in Fig. 8). In addition, as it will be shown in time-domain tests, a poorly damped mode 5C causes considerable rotor voltage oscillations. Again, the selection of the parameter σ_p is a trade-off between avoiding the interaction of the compensation filter with the electrical network and reducing SSOs (i.e., between preventing a poorly damped mode 5C and increasing the damping of the mode 1C). In Fig. 8, this trade-off is seen in the movement in opposite directions of the modes 1C and 5C.

Note that the parameter σ_z is not effective to damp the mode 5C, whereas the parameter σ_p is able to significantly increase the damping ratio of this mode. Thus, the parameter σ_z is chosen first to damp the mode 6C to a desired damping ratio; then, the parameter σ_p is chosen to damp the mode 5C, which improves the rotor voltage response.

In following sections, it will be shown that both a good trade-off and a high performance are obtained by using the values $\sigma_z = 100$ and $\sigma_p = 25$; the parameters of the rotor current controller are $K_p = 0.126$, $K_i = 2.94$, and $K_{ic} = 6.81$, obtained by the LQR method [29] with weighting matrices $\mathbf{Q} = [\ 0.015 \;\; j\,0.325;\ \ -j\,0.325 \;\; 55\ ]$ and $R = 1$ using the MATLAB Control Toolbox. In the controller design, the DFIG model in per-unit values on the machine base is used, so that the control parameters are independent of the DFIG rating, simplifying the control implementation in multi-machine systems with different DFIG rated power.

C. Performance Assessment

Fig. 9 shows the performance comparison of the analyzed cases over a wide range of operating conditions. The system eigenvalues are calculated for 1000 operating points corresponding to a wind power from low to high wind speeds, a series compensation level of the transmission line from 25% to 85%, and a voltage of the network bus from 0.85 pu to 1.15 pu. In the BASE case, several operating points have an unstable subsynchronous mode (see the modes 1A with a positive real part), whereas in the DDF case, the subsynchronous modes are moved toward the left, increasing their damping [see the modes 1C in Fig. 9(a)]; the rest of the eigenvalues also remain well damped for all the operating points, including the key modes 5C and 6C analyzed in the previous section. The SDF case has operating points with the mode 5C very close to the imaginary axis (predicting poorly damped oscillations), whereas in the DDF case, these modes have a more negative real part (i.e., higher damping ratio) [compare the location of the modes 5C in Fig. 9(b)]. As described in Fig. 8, the damping of the mode 1C is slightly reduced in the DDF case compared to the SDF case. This aspect and the impact of the mode 5C on the rotor voltage response are analyzed in the following test.

To obtain the time-domain response of the different control approaches, a 100-ms three-phase fault is applied at the high-voltage side of the substation transformer. Fig. 10 shows the DFIG rotor current for four operating conditions. In agreement with the eigenvalue analysis, the BASE case is prone to poorly damped or even unstable oscillations, particularly for a low output power (low wind condition) and high series compensation levels, whereas the DDF case has a well-damped response for all the scenarios. Fig. 11 shows the response of the SDF and DDF cases. The SSO damping improvement is almost the same in both cases, and the small damping reduction of the mode 1C in the DDF case is practically not distinguished [compare rotor currents in Fig. 11(a)]. On the other hand, in the SDF case, a poorly damped oscillation is observed in the rotor voltage [see Fig. 11(b)]. The frequency of this voltage oscillation is associated with the one of the mode 5C. This oscillation is reduced in the DDF case due to the higher damping of the mode 5C achieved by the introduction of the parameter σ_p. The impact of the mode 5C on the rotor voltage dynamics and the advantage of the compensation filter with double damping terms are more evident in the following multi-machine case study.

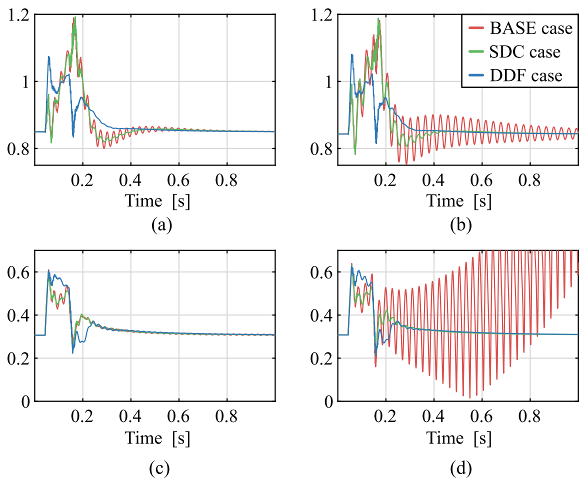

Fig. 10. Rotor current response to a network fault. BASE, SDC, and DDF cases are shown with red, green, and blue lines, respectively. In subplots (a) and (b), the wind farm operates at the maximum power; in subplots (c) and (d), it operates at the minimum power. In subplots (a) and (c), the transmission line is compensated at 35%; in subplots (b) and (d), it is compensated at 70%.

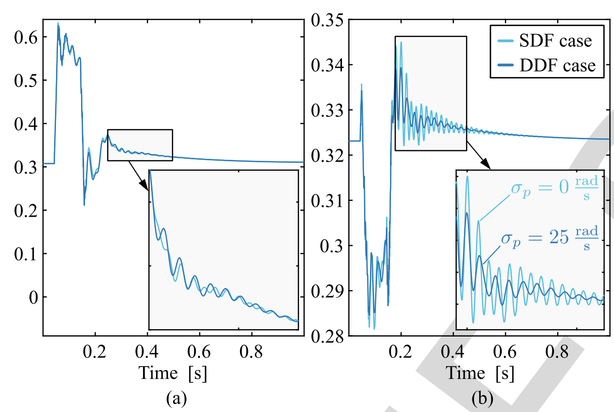

Fig. 11. System response to a network fault. SDF and DDF cases are shown with light-blue and blue lines, respectively. The wind farm operates at the minimum power, and the transmission line is compensated at 70%.

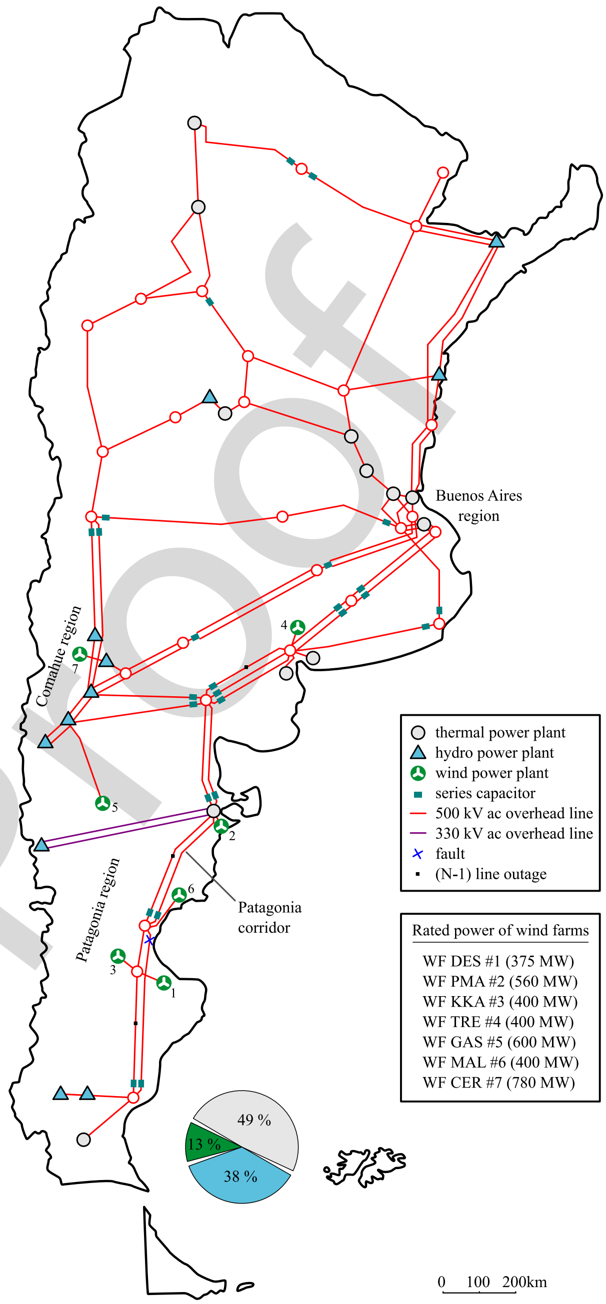

Fig. 12. Single-line diagram of the multi-machine case study based on a future scenario of the Argentinian power system.

V. Multi-Machine Case Study

In this section, the control strategy is verified in a practical case study based on the Argentinian power system (see Fig. 12). The system has 79 buses, 94 transmission lines, 7 DFIG-based wind farms (represented as shown in Fig. 5), and 23 synchronous generators equipped with automatic voltage regulator, power system stabilizer, and turbine-governor system. Thermal generators connected to series-compensated lines have a multi-mass shaft model. Transmission lines and electrical machines are represented by detailed electromagnetic models used in subsynchronous resonance studies (modeling details of the different components can be found in [30] and [32]).

A. Small-Signal Stability Analysis

The proposed control strategy (DDF case) is implemented in all the wind farms of Fig. 12 using the parameters given in Section IV-B. Fig. 13 shows the system eigenvalues of the BASE and DDF cases for 1000 operating points corresponding to different wind power dispatches covering from low to high wind speeds in each wind farm. The case study has three critical subsynchronous modes labeled as 1A′, 1A″, and 1A‴ for the BASE case and 1C′, 1C″, and 1C‴ for the DDF case (see zoom in Fig. 13). In the DDF case, the three subsynchronous modes are moved toward the left, significantly increasing the damping ratio. The SSO damping improvement occurs for all the operating points, even for the unstable points observed in the BASE case. Other key modes such as the modes 5C and 6C are well damped and located in areas very close to the ones shown in the introductory case study, indicating a good

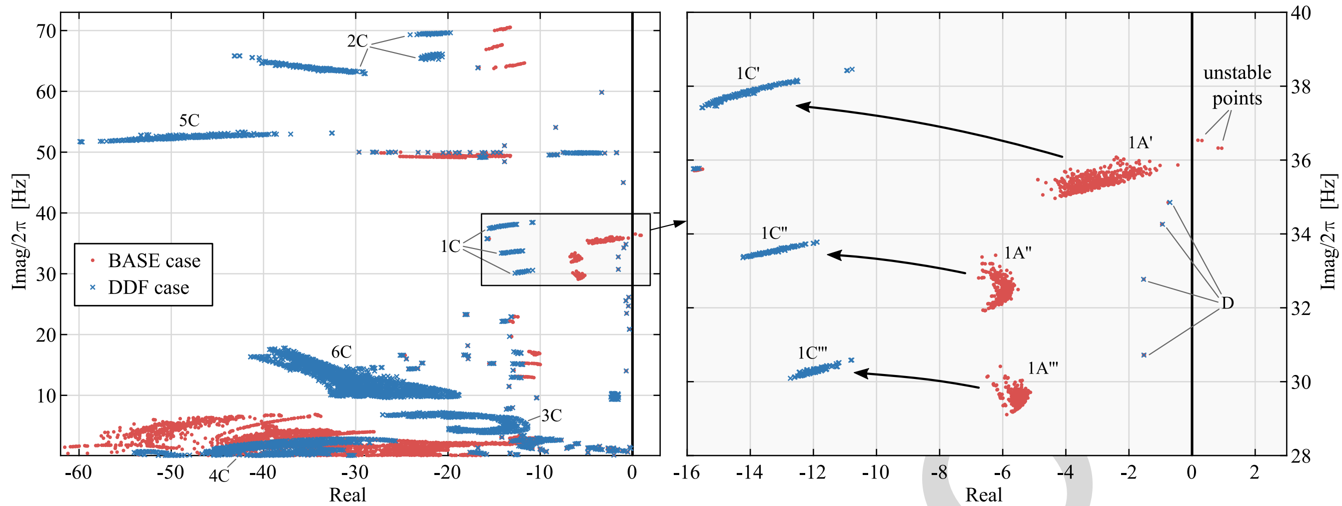

Fig. 13. System eigenvalues calculated for 1000 operating points corresponding to different wind power dispatches. BASE and DDF cases are shown with red dots and blue crosses, respectively. Eigenvalues denoted by D indicate the torsional modes of synchronous generator shafts.

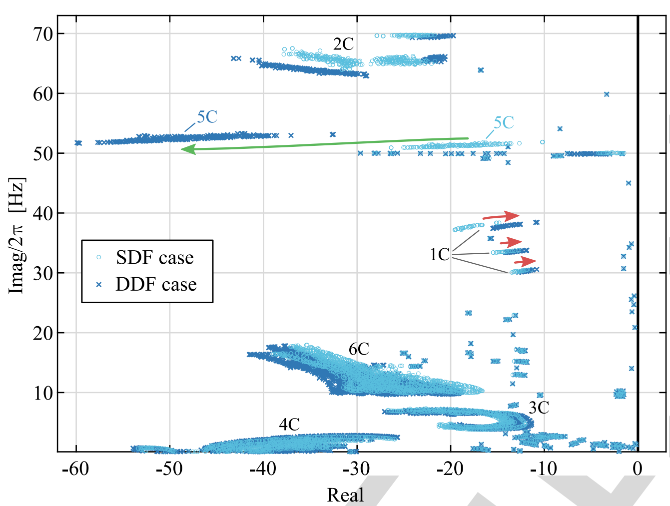

Fig. 14. System eigenvalues calculated for 1000 operating points corresponding to different wind power dispatches. SDF and DDF cases are shown with light-blue circles and blue crosses, respectively.

correlation between the analysis performed in Section IV and the one performed in this more realistic system.

Fig. 14 shows the eigenvalues of the previous test for the SDF and DDF cases. In the DDF case, it is observed a significant increase of the negative real part (damping ratio) of the modes 5C and a slight damping reduction of the modes 1C (see the large green arrow and the small red arrows in Fig. 14). The damping ratio of the mode 5C is critical to achieve a well-damped rotor voltage response (see Section V-D).

B. Robustness Evaluation

In Fig. 15, the eigenvalue test of Section V-A is repeated for eight different scenarios. Scenario 1 represents the nominal case. Scenarios 2, 3, and 4 correspond to $N-1$ line outages (see the lines indicated with black squares in Fig. 12). The out-of-service condition of one of the synchronous generators near the wind farm #4 and the one near the wind farm #2 is given in scenarios 5 and 6, respectively. Scenarios 7 and 8 represent cases where one-half of the wind turbines in the wind farm #5 and one-third of the wind turbines in the wind farm #6 are not in operation. Note that the area where the subsynchronous modes 1C are located is moved toward the left by the SSCI countermeasure, consequently increasing the SSO damping (compare the location of the dashed line squares for the BASE and DDF cases in Fig. 15). This result is observed for all the scenarios, thus confirming the robustness of the control strategy.

C. Time-Domain Tests

In Fig. 16, the system is operating with the Patagonia corridor compensated at 35%; at 0.1 s, the compensation level is increased to 70% by connecting series capacitor banks, reaching one of the critical points where the BASE case is unstable (see zoom in Fig. 13). As expected, in the BASE case, ac-bus voltages and rotor voltages show growing SSOs after the capacitor connection. On the other hand, these voltages are quickly damped by the action of the compensation filter in the SDF and DDF cases. These two cases have a similar performance in terms of SSO damping, but there are differences in the additional control effort required by the SSO damping action. This topic will be analyzed in the next section.

D. Magnitude of the Rotor Voltage

The maximum voltage that the rotor-side converter is able to synthesize without reaching the overmodulation region is given by

$$|v_r|^{\max} = \frac{N_s v_{dc}}{\sqrt{2} N_r V_N}. \tag{24}$$

Considering the DFIG parameters: stator/rotor turns ratio $N_s/N_r = 0.333$, dc-link voltage $v_{dc} = 1300$ V, and nominal RMS line-to-line voltage $V_N = 690$ V, the maximum magnitude of the rotor voltage is 0.44 pu (in dq coordinates).

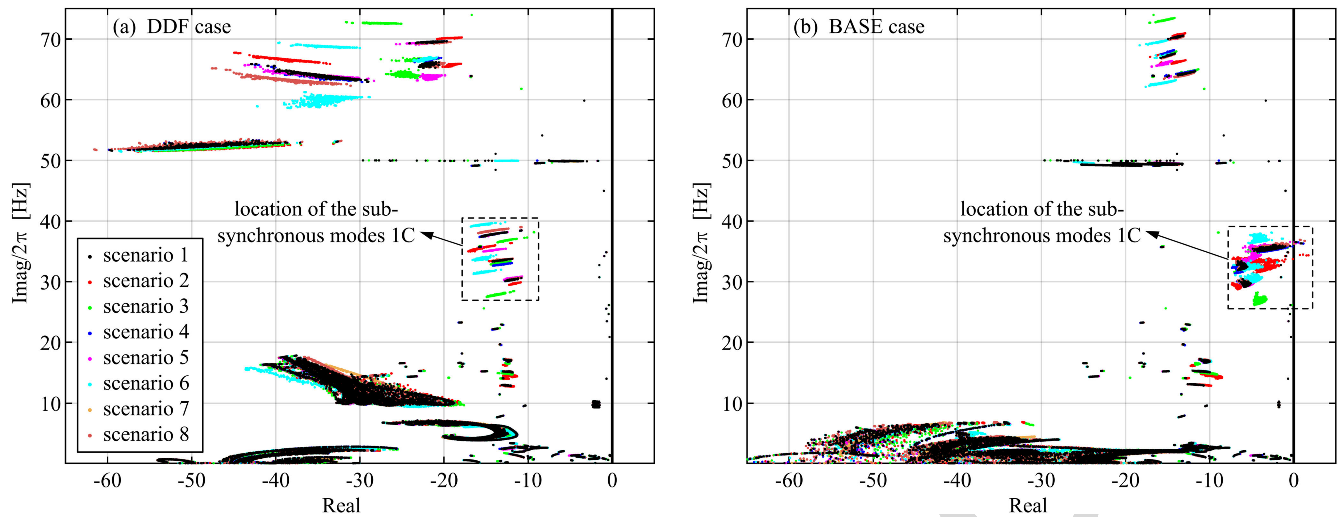

Fig. 15. System eigenvalues calculated for 1000 operating points corresponding to different wind power dispatches. Scenarios considering different contingencies are shown with different colors. DDF and BASE cases are shown in the first and second column, respectively.

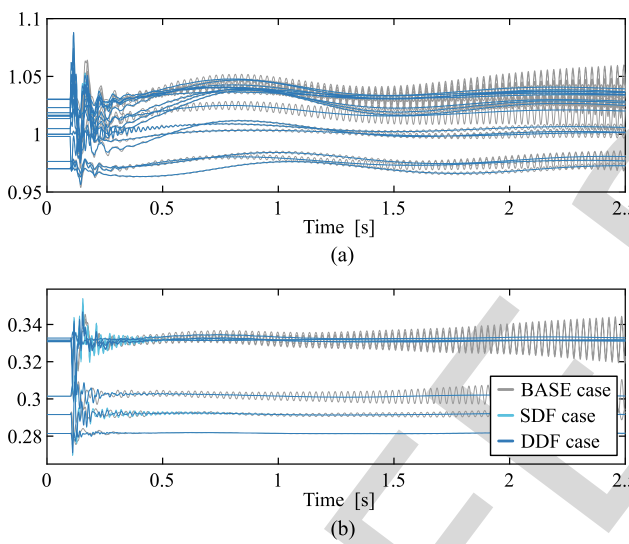

Fig. 16. Test increasing the series compensation level of the Patagonia corridor from 35% to 70%. BASE, SDF, and DDF cases are shown with gray, light-blue, and blue lines, respectively. (a) voltages of the ac buses of the Patagonia corridor and (b) DFIG rotor voltages.

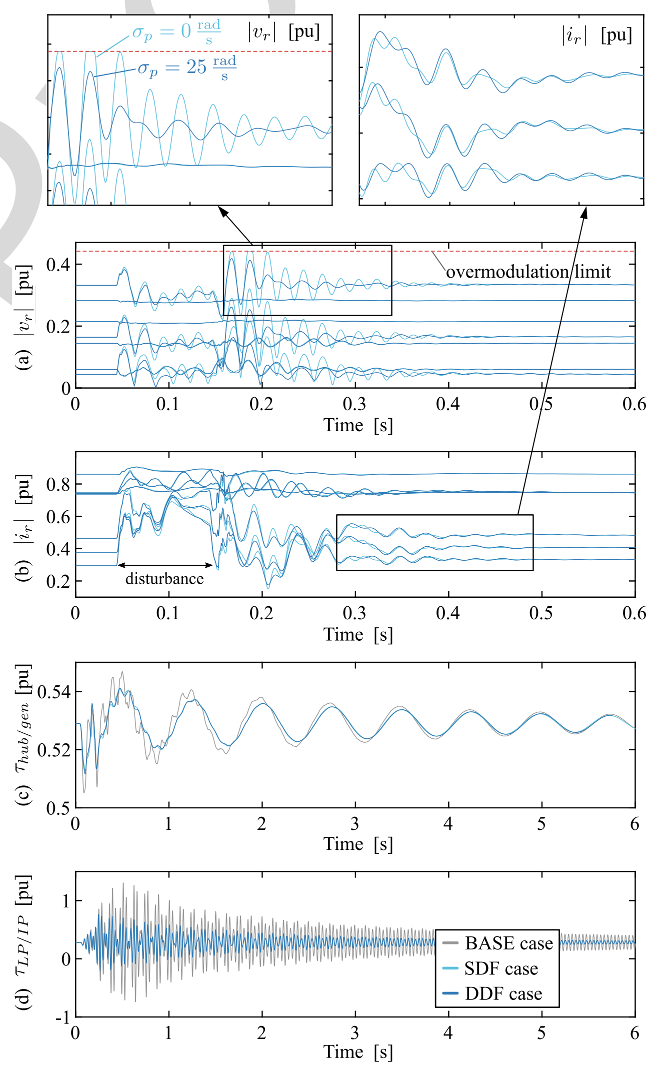

Fig. 17. System response to a network fault. (a) rotor voltages, (b) rotor currents, (c) hub/generator shaft torque of the WF #2, and (d) LP/IP shaft torque of the synchronous generator near WF #2.

The system response to a three-phase fault is shown in Fig. 17 (see the fault location in Fig. 12). The fault is cleared by tripping the faulted line. A larger overshoot and oscillation of rotor voltages are seen in the SDF case compared to the DDF case [see Fig. 17(a)]. As described in Section IV, the increase of the parameter σ_p reduces the rotor voltage oscillations (associated with the mode 5C) and diminishes the SSO damping (associated with the mode 1C). However, the increase in the damping of the mode 5C has a significant improvement in the rotor voltage response [compare the SDF and DDF cases in Fig. 17(a)], whereas the slightly lower damping of the subsynchronous mode 1C is barely noted in the rest of the system variables [e.g., see rotor currents in Fig. 17(b)]; thus, the selected σ_p value achieves a good trade-off. Both the SDF and DDF approaches are able to mitigate SSCI, but the compensation filter with double damping terms provides the designer the freedom to improve the rotor voltage dynamics. Finally, mechanical variables are compared by showing shaft torques of a wind turbine and a synchronous generator [see Figs. 17(c) and (d)]. Almost the same response is seen in the SDF and DDF cases (light-blue and blue lines, respectively), with an improvement over the BASE case (gray line). No mechanical stability problems are observed.

VI. Conclusion

An enhanced compensation filter based on the MIA concept was proposed to mitigate SSOs in DFIG-based wind farms. The additional degree of freedom of the filter allows adjusting the rotor voltage and prevents the converter overmodulation due to the SSO damping action. The proposed control strategy acts locally on the electrical machine reducing its negative damping in the subsynchronous frequency range and dealing directly with the root of the SSO problem. Therefore, the control strategy has a low dependence on the network parameters and the system operating point. The SSO mitigation strategy was validated with a practical case study based on the Argentinian power system and evaluated in a wide range of operating conditions by extensive eigenvalue analysis and nonlinear time-domain simulations. The obtained results show that the DFIG control system can be updated to avoid poorly damped SSOs when DFIG-based wind farms are integrated into series-compensated transmission systems.

References

[1] G. Irwin, A. Jindal, and A. Isaacs, "Sub-synchronous control interactions between type 3 wind turbines and series compensated AC transmission systems," in *Proc. IEEE Power Energy Soc. Gen. Meeting*, Jul. 2011, pp. 1–6.

[2] X. Xie, Y. Zhan, J. Shair, Z. Ka, and X. Chang, "Identifying the source of subsynchronous control interaction via wide-area monitoring of sub/super-synchronous power flows," *IEEE Trans. Power Del.*, vol. 35, no. 5, pp. 2177–2185, Oct. 2020.

[3] L. Wang, X. Xie, Q. Jiang, H. Liu, Y. Li, and H. Liu, "Investigation of SSR in practical DFIG-based wind farms connected to a series-compensated power system," *IEEE Trans. Power Syst.*, vol. 30, no. 5, pp. 2772–2779, Sep. 2015.

[4] M. T. Ali, D. Zhou, Y. Song, M. Ghandhari, L. Harnefors, and F. Blaabjerg, "Analysis and mitigation of SSCI in DFIG systems with experimental validation," *IEEE Trans. Energy Convers.*, vol. 35, no. 2, pp. 714–723, Jun. 2020.

[5] U. Karaagac, J. Mahseredjian, S. Jensen, R. Gagnon, M. Fecteau, and I. Kocar, "Safe operation of DFIG-based wind parks in series-compensated systems," *IEEE Trans. Power Del.*, vol. 33, no. 2, pp. 709–718, Apr. 2018.

[6] A. E. Leon and J. A. Solsona, "Sub-synchronous interaction damping control for DFIG wind turbines," *IEEE Trans. Power Syst.*, vol. 30, no. 1, pp. 419–428, Jan. 2015.

[7] J. Shair, X. Xie, L. Wang, W. Liu, J. He, and H. Liu, "Overview of emerging subsynchronous oscillations in practical wind power systems," *Renewable Sustain. Energy Rev.*, vol. 99, pp. 159–168, 2019.

[8] H. Liu, X. Xie, X. Gao, H. Liu, and Y. Li, "Stability analysis of SSR in multiple wind farms connected to series-compensated systems using impedance network model," *IEEE Trans. Power Syst.*, vol. 33, no. 3, pp. 3118–3128, May 2018.

[9] P. Mahish and A. K. Pradhan, "Mitigating subsynchronous resonance using synchrophasor data based control of wind farms," *IEEE Trans. Power Del.*, vol. 35, no. 1, pp. 364–376, Feb. 2020.

[10] J. Shair, X. Xie, and G. Yan, "Mitigating subsynchronous control interaction in wind power systems: Existing techniques and open challenges," *Renewable Sustain. Energy Rev.*, vol. 108, pp. 330–346, 2019.

[11] X. Zhang, X. Xie, J. Shair, H. Liu, Y. Li, and Y. Li, "A grid-side subsynchronous damping controller to mitigate unstable SSCI and its hardware-in-the-loop tests," *IEEE Trans. Sustain. Energy*, vol. 11, no. 3, pp. 1548–1558, Jul. 2020.

[12] H. Liu, X. Xie, Y. Li, H. Liu, and Y. Hu, "Mitigation of SSR by embedding subsynchronous notch filters into DFIG converter controllers," *IET Gener. Transmiss. Distrib.*, vol. 11, no. 11, pp. 2888–2896, 2017.

[13] Y. Li, L. Fan, and Z. Miao, "Replicating real-world wind farm SSR events," *IEEE Trans. Power Del.*, vol. 35, no. 1, pp. 339–348, Feb. 2020.

[14] H. A. Mohammadpour, A. Ghaderi, H. Mohammadpour, and E. Santi, "SSR damping in wind farms using observed-state feedback control of DFIG converters," *Elect. Power Syst. Res.*, vol. 123, pp. 57–66, 2015.

[15] U. Karaagac, S. Faried, J. Mahseredjian, and A.-A. Edris, "Coordinated control of wind energy conversion systems for mitigating subsynchronous interaction in DFIG-based wind farms," *IEEE Trans. Smart Grid*, vol. 5, no. 5, pp. 2440–2449, Sep. 2014.

[16] X. Bian, Y. Ding, Q. Jia, L. Shi, X. Zhang, and K. L. Lo, "Mitigation of sub-synchronous control interaction of a power system with DFIG-based wind farm under multi-operating points," *IET Gener. Transmiss Distrib.*, vol. 12, no. 21, pp. 5834–5842, 2018.

[17] J. Yao, X. Wang, J. Li, R. Liu, and H. Zhang, "Sub-synchronous resonance damping control for series-compensated DFIG-based wind farm with improved particle swarm optimization algorithm," *IEEE Trans. Energy Convers.*, vol. 34, no. 2, pp. 849–859, Jun. 2019.

[18] A. E. Leon, "Integration of DFIG-based wind farms into series-compensated transmission systems," *IEEE Trans. Sustain. Energy*, vol. 7, no. 2, pp. 451–460, Apr. 2016.

[19] C. Karunanayake, J. Ravishankar, and Z. Y. Dong, "Nonlinear SSR damping controller for DFIG based wind generators interfaced to series compensated transmission systems," *IEEE Trans. Power Syst.*, vol. 35, no. 2, pp. 1156–1165, Mar. 2020.

[20] J. Shair, X. Xie, Y. Li, and V. Terzija, "Hardware-in-the-loop and field validation of a rotor-side subsynchronous damping controller for a DFIG connected to a series compensated line," *IEEE Trans. Power Del.*, to be published. Q3

[21] H. J. Baesmat and M. Bodson, "Suppression of sub-synchronous resonances through excitation control of doubly fed induction generators," *IEEE Trans. Power Syst.*, vol. 34, no. 6, pp. 4329–4340, Nov. 2019.

[22] M. Ghafouri, U. Karaagac, H. Karimi, S. Jensen, J. Mahseredjian, and S. O. Faried, "An LQR controller for damping of subsynchronous interaction in DFIG-based wind farms," *IEEE Trans. Power Syst.*, vol. 32, no. 6, pp. 4934–4942, Nov. 2017.

[23] M. Ghafouri, U. Karaagac, J. Mahseredjian, and H. Karimi, "SSCI damping controller design for series-compensated DFIG-based wind parks considering implementation challenges," *IEEE Trans. Power Syst.*, vol. 34, no. 4, pp. 2644–2653, Jul. 2019.

[24] P.-H. Huang, M. El Moursi, W. Xiao, and J. Kirtley, "Subsynchronous resonance mitigation for series-compensated DFIG-based wind farm by using two-degree-of-freedom control strategy," *IEEE Trans. Power Syst.*, vol. 30, no. 3, pp. 1442–1454, May 2015.

[25] H. Ghaffarzdeh and A. Mehrizi-Sani, "Mitigation of subsynchronous resonance induced by a type III wind system," *IEEE Trans. Sustain. Energy*, vol. 11, no. 3, pp. 1717–1727, Jul. 2020.

[26] Y. Gu, J. Liu, T. C. Green, W. Li, and X. He, "Motion-induction compensation to mitigate sub-synchronous oscillation in wind farms," *IEEE Trans. Sustain. Energy*, vol. 11, no. 3, pp. 1247–1256, Jul. 2020.

[27] L. Fan and Z. Miao, "Nyquist-stability-criterion-based SSR explanation for type-3 wind generators," *IEEE Trans. Energy Convers.*, vol. 27, no. 3, pp. 807–809, Sep. 2012.

[28] A. I. Semlyen, "s-domain methodology for assessing the small signal stability of complex systems in nonsinusoidal steady state," *IEEE Trans. Power Syst.*, vol. 14, no. 1, pp. 132–137, Feb. 1999.

[29] K. Ogata, *Modern Control Engineering*. Englewood Cliffs, NJ, USA: Prentice-Hall, 1997.

[30] O. Anaya-Lara, N. Jenkins, J. Ekanayake, P. Cartwright, and M. Hughes, *Wind Energy Generation: Modelling Control.*: Hoboken, NJ, USA: Wiley, 2009.

[31] F. Milano, *Power System Modelling and Scripting, Power Systems*. Berlin, Germany: Springer-Verlag, 2010.

[32] P. Kundur, *Power System Stability and Control*. New York, NY, USA: McGraw-Hill, 1994.